Quantitative proteomic analysis reveals apoE4-dependent phosphorylation of the actin-regulating protein VASP

Zeynep Cakir[1,2,3], Samuel J. Lord[2,4], David Jimenez-Morales[1,2,3,5], Gwendolyn M. Jang[1,2,3], Benjamin J. Polacco[1,2,3], Manon Eckhardt[1,2,3], Billy W. Newton[1,2,3], Yuan Zhou[1,2,3], Adam L. Orr[6,7], Jeffrey R. Johnson[1,2,3,8], R. Dyche Mullins[2,4], Nevan J. Krogan[1,2,3], Robert W. Mahley[6,9], Danielle L. Swaney[1,2,3,*]

[1]University of California San Francisco, Quantitative Biosciences Institute (QBI), San Francisco, CA, 94158, USA.
[2]University of California San Francisco, Department of Cellular and Molecular Pharmacology, San Francisco, CA, 94143, USA.
[3]Gladstone Institute of Data Science and Biotechnology, Gladstone Institutes, San Francisco, CA, 94158, USA.
[4]Howard Hughes Medical Institute, San Francisco, CA, 94143, USA.
[5]Current address: Department of Medicine, Division of Cardiovascular Medicine, Stanford University, Stanford, CA, USA
[6]Gladstone Institute of Neurological Disease, Gladstone Institutes, San Francisco, CA, 94158, USA.
[7]Current address: Helen and Robert Appel Alzheimer's Disease Research Institute, Feil Family Brain and Mind Research Institute, Weill Cornell Medicine, New York, NY, 10021, USA.
[8]Current address: Department of Microbiology, Icahn School of Medicine at Mount Sinai, New York, NY, 10029, USA.
[9]University of California San Francisco, Departments of Pathology and Medicine, San Francisco, CA, 94143, USA.

*Correspondence: danielle.swaney@ucsf.edu (DLS)

Abstract
Apolipoprotein (apo) E4 is the major genetic risk factor for Alzheimer's Disease (AD). While neurons generally produce a minority of the apoE in the central nervous system, neuronal expression of apoE increases dramatically in response to stress and is sufficient to drive pathology. Currently, the molecular mechanisms of how apoE4 expression may regulate pathology are not fully understood. Here we expand upon our previous studies measuring the impact of apoE4 on protein abundance to include the analysis of protein phosphorylation and ubiquitylation signaling in isogenic Neuro-2a cells expressing apoE3 or apoE4. ApoE4 expression resulted in a dramatic increase in VASP S235 phosphorylation in a PKA-dependent manner. This phosphorylation disrupted VASP interactions with numerous actin cytoskeletal and microtubular proteins. Reduction of VASP S235 phosphorylation via PKA inhibition resulted in a significant increase in filopodia formation and neurite outgrowth in apoE4-expressing cells, exceeding levels observed in apoE3-expressing cells. Our results highlight the pronounced and diverse impact of apoE4 on multiple modes of protein regulation and identify potential therapeutic targets to restore apoE4-related cytoskeletal defects.

Introduction
Apolipoprotein (apo) E is the major cholesterol transport protein in the brain and exists as three allelic variants, apoE2, apoE3, and apoE4, which each differ by single amino acid interchanges (Mahley, 1988; Mahley et al., 2006, 2009). The apoE4 variant is the major genetic risk factor for Alzheimer's disease (AD) (Corder et al., 1993; Farrer et al., 1997; Genin et al., 2011), occuring in 60–70% of all sporadic and familial AD cases (Corder et al., 1993; Farrer et al., 1997; Genin et al., 2011; Mahley et al., 2006). ApoE4 lowers the age of onset and increases the risk of developing AD, and considerable evidence indicates that apoE4 has a fundamental role in AD neurodegeneration (Biundo et al., 2015; Bu, 2009; Holtzman et al., 2012; Huang and Mucke, 2012; Kim et al., 2009; Liu et al., 2013; Mahley and Huang, 2012a, 2012b; Mahley et al., 2006, 2009; Spinney, 2014). However, the precise molecular mechanisms by which apoE4 drives pathology remain unclear (Koutsodendris et al., 2021; Martens et al., 2022).

Current evidence suggests that neuronal expression of apoE4 is important to this process. Though neurons produce a minority of the apoE in the central nervous system (~20%) (Knoferle et al., 2014), neuronal apoE expression levels increase dramatically in response to stress via a neuron-specific splicing mechanism (Xu et al., 2008). Furthermore, neuronal expression of apoE4 is sufficient to drive pathology (Huang and Mucke,

2012; Knoferle et al., 2014; Mahley and Huang, 2012a; Mahley et al., 2006; Tong et al., 2014), likely via an apoE4 gain-of-function mechanism as compared to apoE3 (Wang et al., 2018).

Numerous studies have shown that apoE4-driven neuropathology is associated with a variety of cellular phenotypes, including mitochondrial dysfunction (Atamna and Frey, 2007; Orr et al., 2019; Parihar and Brewer, 2007), cytoskeletal defects and altered microtubule structure (Mahley and Huang, 2012a). Remarkably, apoE4 expression increases phosphorylation of the microtubule-associated protein tau by activating the Erk pathway in the hippocampus of Neuron-Specific Enolase (NSE)-apoE transgenic mice and in cultured neuronal cells (Harris et al., 2004). Furthermore, apoE4 induces neurofibrillary tangle (NFT) structures that include phosphorylated tau protein (Harris et al., 2003). Treatment of cultured neuronal cells with apoE4-lipid complexes impairs neurite outgrowth compared to apoE3-lipid complexes (Bellosta et al., 1995; Nathan et al., 1994, 1995). Likewise, neuroblastoma cells stably expressing apoE4 display impaired neurite outgrowth; however this can be restored by site-directed mutagenesis of apoE4 or by treatment with small molecule structure correctors that convert the apoE4 structure to one that resembles apoE3 (Brodbeck et al., 2011; Chen et al., 2012).

Unbiased global proteomic analysis of protein abundance and post-translational modifications (PTMs) by mass spectrometry (MS) represents a powerful mechanism to discover regulatory biological mechanisms. However, to date, efforts to identify the proteomic impact of apoE4 by MS have primarily been focused on specific organelles or subcompartments (James et al., 2012; Shi et al., 2014), and have identified few differentially regulated proteins. Recently, we reported a global protein abundance analysis of Neuro-2a cells expressing apoE3 or apoE4 revealing hundreds of differentially regulated proteins and correlating these differences to apoE4-specific cellular processes (Orr et al., 2019). To further our understanding of the molecular mechanisms that may regulate apoE4-specific pathology, we have expanded upon our previous studies to include the analysis of protein phosphorylation and ubiquitylation signaling in isogenic Neuro-2a cells expressing human apoE3 or apoE4. The results highlight the diverse impact of apoE4 on multiple modes of protein regulation and identify a mechanism of apoE4-mediated cytoskeletal biology.

Results

Post-translational modification networks are highly regulated by apoE4. Our previous work has shown that apoE allele status can significantly regulate the proteome, resulting in mitochondrial dysfunction and altered cellular metabolism (Orr et al., 2019). To further define the proteomic impact of apoE4, we analyzed differences for thousands of protein phosphorylation and ubiquitylation sites between isogenic mouse Neuro-2a cells expressing human apoE3 or apoE4 (**Fig. 1 A-B, Table S1**). These neuron-like cells have been extensively characterized and shown to recapitulate numerous phenotypes observed in AD patients, including increased Amyloid β (Aβ) (Huang and Mucke, 2012), tau hyperphosphorylation and NFTs (Huang et al., 2001), and mitochondrial dysfunction (Orr et al., 2019). Additionally, we found that apoE4 expression in Neuro-2a cells resulted in depletion of proteins normally expressed in brain regions that incur neuronal loss in AD patients, including the hippocampus (FDR = 3.3×10^{-3}) and the temporal lobe (FDR = 3.3×10^{-3}) (Lee and Maguire, 2014; Lucas and Clem, 2018; Szklarczyk et al., 2019; Zhao et al., 2020), further supporting the relevance of these cells as an AD model.

Our proteomics analyses revealed dramatic rewiring of cellular signaling across multiple modes of regulation, resulting in differential regulation of thousands of proteins and PTM sites (**Fig. 1C, Fig. S1**). While there was a high degree of overlap in the proteins detected across data types, we observed apoE allele regulation to impact highly unique subsets of the proteome (**Fig. 1D**), as has been observed in the analysis of AD patient brain tissue (Bai et al., 2020). To investigate the function of differentially regulated proteins and PTMs on a pathway level, we performed gene ontology (GO) enrichment analysis (**Fig. 1E, Table S2**). This showed that while > 1000 ubiquitylated peptides were differentially regulated, few ontology terms were highly enriched, suggesting that ubiquitylation changes were not coordinated on proteins representing well annotated processes, functions, or cellular compartments. In contrast, we found several highly enriched ontology terms among the differentially phosphorylated proteins, including greater phosphorylation on chromatin binding proteins in apoE4 cells, and less abundant phosphorylation in apoE4 cells for proteins involved in processes such as regulation of the cytoskeleton and signal transduction, including Ras protein signal transduction. Of

note, the protein abundance analysis also revealed a highly significant decrease in proteins associated with the cytoskeleton in apoE4 Neuro-2a cells.

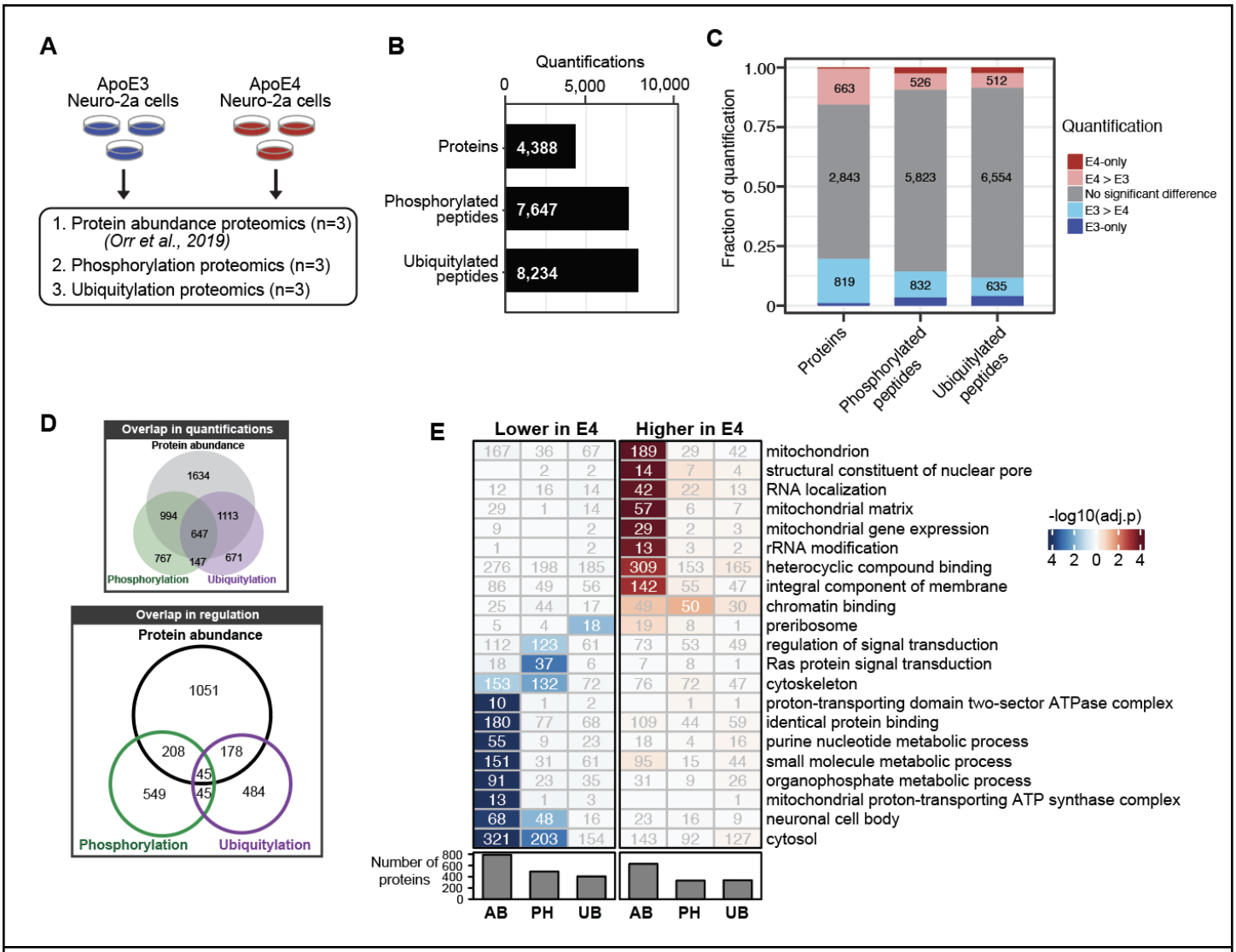

Figure 1. Experimental overview. In all panels, differential regulation is defined as proteins or PTMs with $p < 0.05$. (**A**) ApoE3 and apoE4 Neuro-2a cells were subjected to proteomic analysis in biological triplicate, measuring protein abundance (data previously reported (Orr et al., 2019)), phosphorylated peptides, and ubiquitylated peptides. (**B**) Total number of unique quantifications for each analysis method. (**C**) Fraction of differentially regulated qualifications for each analysis method. When a peptide or protein was only detected in one cell type it was designated as E3-only or E4-only. Values within the bars indicate the number of proteins or peptides represented for different quantification classification groups. (**D**) Overlap of proteins or PTM-containing proteins from all quantified proteins/PTMs (top), or only from those proteins/PTMs that were differentially regulated (bottom). (**E**) Gene ontology enrichment analysis. Enrichment analysis was performed on proteins or peptides with $p < 0.05$.

The cytoskeletal protein VASP is phosphorylated at S235 in an apoE4-dependent manner. We hypothesized that the enrichment of cytoskeletal proteins in both the protein abundance and phosphorylation analyses may provide mechanistic insights into the established cytoskeletal defects previously observed in apoE4 cells. Intriguingly, the most significantly regulated phosphorylation site in our data was Vasodilator-stimulated phosphoprotein (VASP) S235, which was 14-fold higher in apoE4 cells (**Fig. 2A**). VASP is a member of the conserved ENA/VASP family of proteins regulating diverse cellular processes such as cell adhesion, neurite initiation, axon outgrowth and actin cytoskeletal dynamics (Döppler and Storz, 2013). We validated the increase in VASP S235 phosphorylation in apoE4 cells by immunoblotting, and found that it occurred without a concomitant increase in VASP protein abundance (**Fig. 2B**). This increase in

phosphorylation was unique to apoE4 expressing cells, as VASP S235 phosphorylation was not detectable in wild-type (WT) Neuro-2a cells that lack apoE expression (**Fig. 2C**). Lastly, to further confirm the role of apoE4 in promoting VASP S235 phosphorylation, we performed siRNA knockdown of apoE and observed up to a 50% reduction in this phosphorylation site in apoE4 cells (**Fig. 2D, S2**).

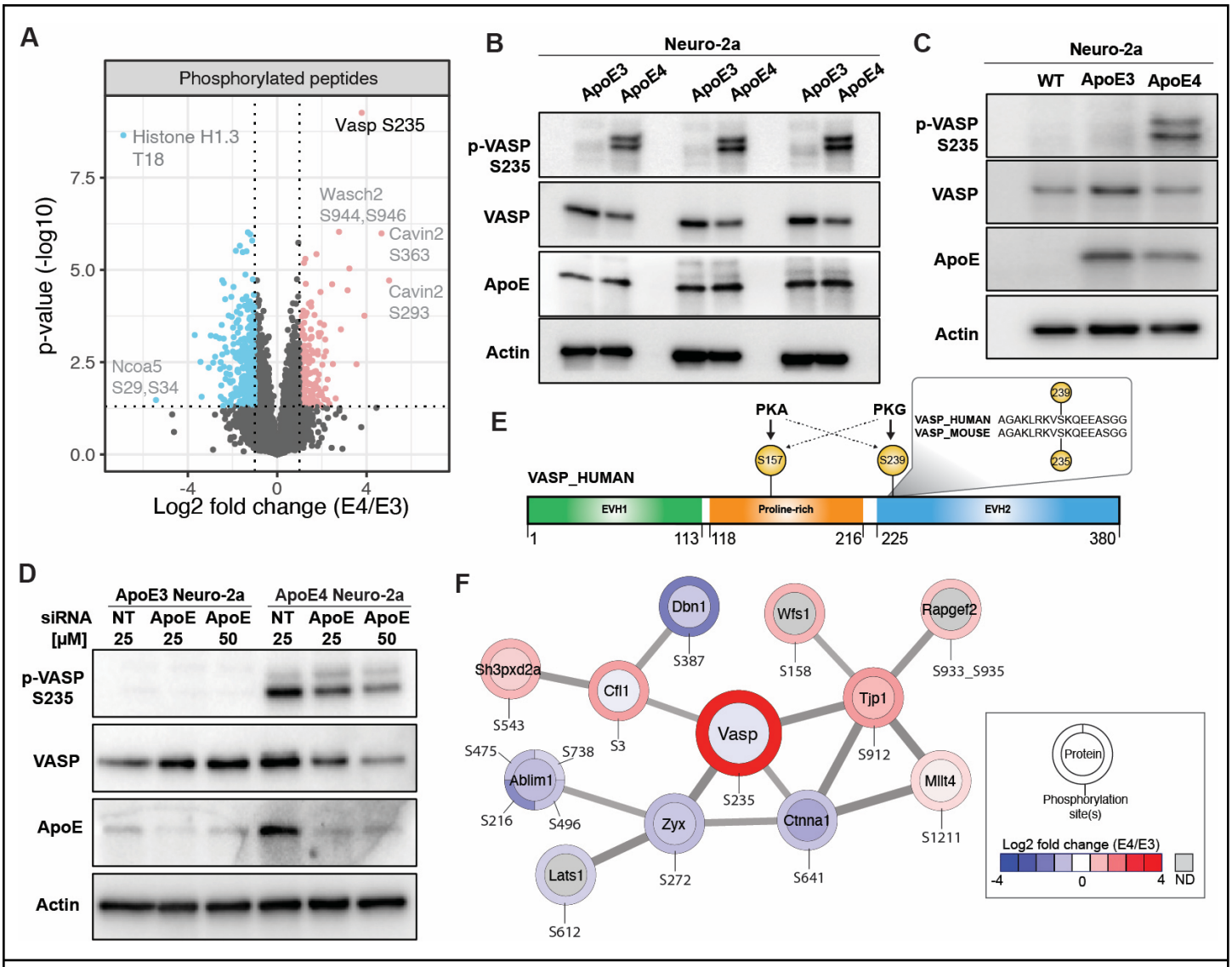

Figure 2. VASP is phosphorylated at S235 in an apoE4-dependent manner. (**A**) Volcano plots for quantified phosphopeptides. Colored data points indicate analytes with $p < 0.05$ and a $\log_2$ fold change > 1. A selection of significantly regulated phosphopeptides are annotated with their gene name and the modified amino acid position. (**B**) Phosphorylation of VASP at S235 in apoE4 Neuro-2a cells validation by immunoblotting (n=3 biological replicates), with actin as a loading control. (**C**) VASP phosphorylation at S235 in Neuro-2a cells in the absence of apoE (WT) or different apoE alleles. Actin serves as a loading control. (**D**) Western blot measuring VASP S235 phosphorylation, VASP protein and apoE protein upon knockdown of apoE with the increasing concentrations of siRNA in apoE3 Neuro-2a and apoE4 Neuro-2a cells. NT indicates a non-targeting siRNA as a negative control. Actin serves as a loading control. (**E**) VASP protein domain organization: EVH1:Ens/VASP Homology 1, Poly-Proline rich domain (PPR), EVH2: Ena/VASP homology 2. VASP proteins are the substrates of PKA or PKG. VASP S235 (mouse) and VASP S239 (human) are conserved across species. (**F**) Quantification of specific phosphorylation sites and protein abundance differences for proteins known to interact with VASP based on the STRING database. Protein abundance quantification is displayed in the interior circle. Phosphorylation site amino acid position and quantification annotations are displayed on the border, ND:not detected.

VASP is composed of three conserved domains: an N-terminal Ena/VASP homology-1 (EVH-1) domain, a central poly-proline rich domain (PPR) and a C-terminal EVH-2 domain (Kwiatkowski et al., 2003; Reinhard et

al., 2001) (**Fig. 2E**). While EVH-1 interacts with proteins such as zyxin and vinculin, which are important for cytoskeletal regulation, the PRR domain mediates the interaction with profilin-actin complexes to enhance actin polymerization (Ferron et al., 2007; Reinhard et al., 2001). Beyond VASP itself, we found that many proteins related to VASP biology were also differentially regulated phosphorylation in apoE4-expressing cells, including zyxin (Zyx), drebrin (Dbn1), actin-binding LIM1 protein (Ablim1) and Cofilin-1 (Cfn1) proteins (**Fig. 2F**). Many of these had previously been linked to AD pathogenesis or nervous system development, including Dbn1 (Harigaya et al., 1996), Cfn1 (Flynn et al., 2009), and Zyx (Gomez et al., 1996; Hoffman et al., 2006; Legerstee et al., 2019; Luo et al., 2014). In line with this, our global proteomic analysis showed that abundance levels of these four proteins are reduced in Neuro-2a apoE4 cells (**Fig. 2F**).

VASP S235 phosphorylation is mediated by PKA. Phosphorylation of VASP at serine 235 (mouse), or the orthologous serine 239 (human), is known to impair F-actin accumulation, cell adhesion, and filopodia formation (Benz et al., 2009) (**Fig. 2E**). The serine threonine kinases PKG and PKA can phosphorylate VASP at S235. PKG is the preferred kinase for this site (Butt et al., 1994), while PKA has been shown to preferentially phosphorylate VASP S157 (**Fig. 2E**) (Döppler and Storz, 2013). In order to understand which protein kinase is responsible for VASP S235 phosphorylation in apoE4 Neuro-2a cells, we first treated cells with two different PGK inhibitors RRKAARE (**Fig. 3A**) or KT5823 (**Fig. S3**); however no decrease in phosphorylation was observed. In contrast, treatment of cells with two different PKA inhibitors, H89 (**Fig. 3B-C**) or KT5720 (**Fig. S3**), both dramatically reduced VASP S235 phosphorylation. These results suggest that PKA is responsible for the majority of VASP S235 phosphorylation and is the preferential kinase for this site in apoE4 Neuro-2a cells.

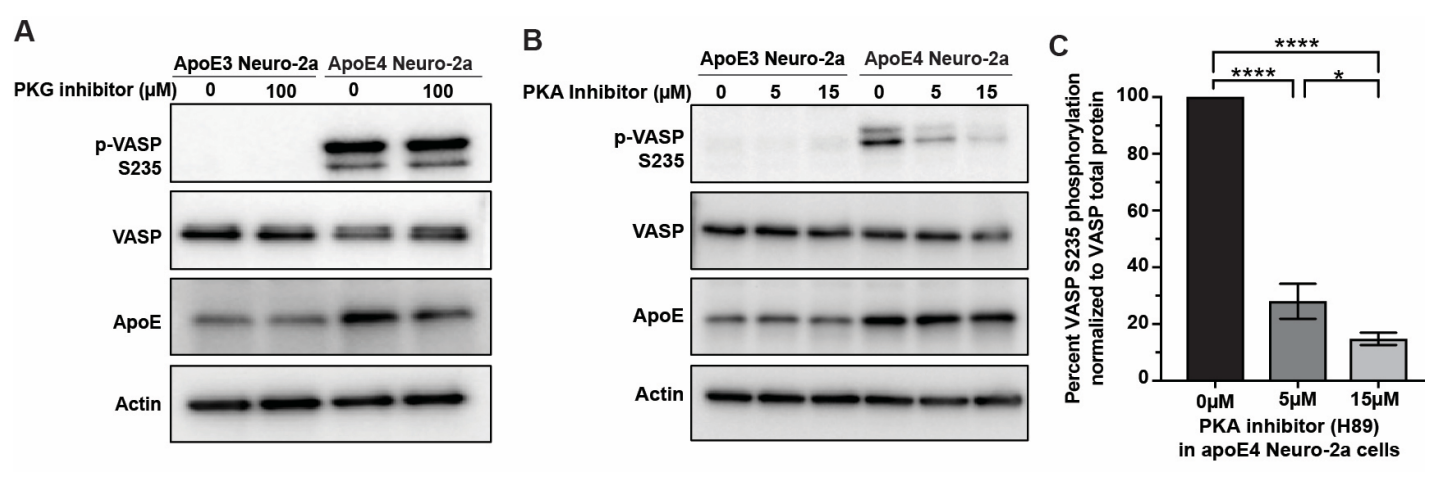

Figure 3. VASP S235 is phosphorylated by PKA. Immunoblots of VASP S235 phosphorylation in apoE3 and apoE4 Neuro-2a cells upon kinase inhibition. (**A**) 24h inhibition with the PKG inhibitor, RKRARKE . (**B**) 24h inhibition with increasing concentrations of the PKA inhibitor H89. Actin serves as a loading control. (**C**) Quantification of VASP S235 phosphorylation levels from panel B. Data are mean ± s.d. from n=3 biological replicates per group * $p<0.05$; **** $p<0.0001$.

VASP interactions with actin cytoskeletal proteins are regulated by PKA. To investigate the role of VASP S235 phosphorylation in apoE4 Neuro-2a cells, we performed affinity purification-mass spectrometry (APMS) to identify how VASP protein-protein interactions (PPIs) are regulated by its phosphorylation status. We expressed wild-type human VASP (hVASP WT), which was highly phosphorylated at the orthologous S239 position in apoE4 Neuro-2a cells (**Fig. S4**), similar to what we observed for the endogenous mouse VASP S235 phosphorylation. Separately, we expressed human VASP with an S239A mutation (hVASP S239A) which prohibits phosphorylation at this position. APMS experiments were performed in the presence or absence of PKA inhibition with H89 (**Fig. 4A**).

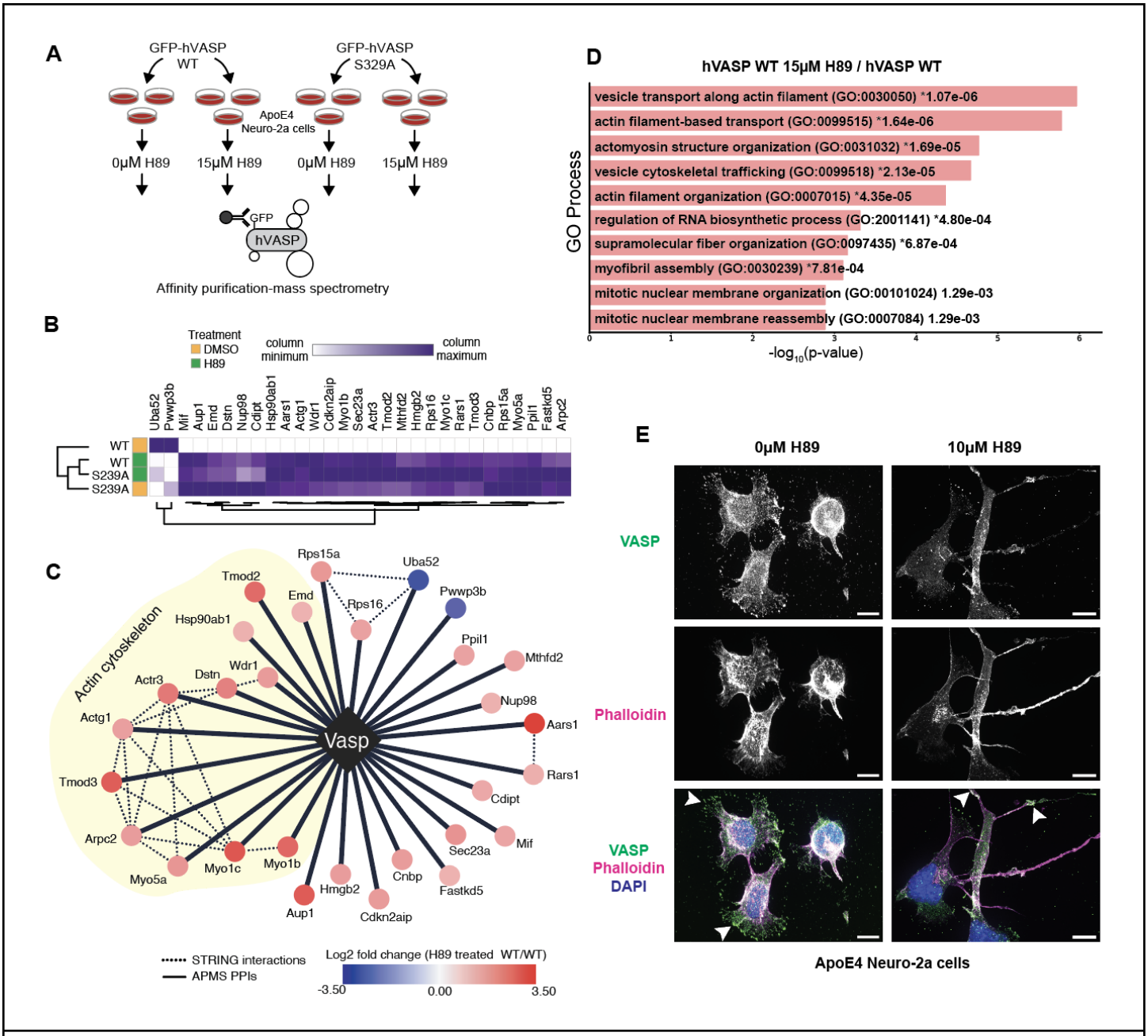

Figure 4. Phosphorylated VASP and phospho-null VASP protein interacting networks. (**A**) GFP-tagged human VASP (hVASP) WT and hVASP S239A are expressed in apoE4 Neuro-2a cells in triplicate in the absence or presence of 15μM H89. GFP is used as a tag to pull down VASP protein interacting partners which were identified using MS. (**B**) Heat map represents scaled protein abundance values for a selection of interacting proteins specifically regulated by hVASP S239 phosphorylation. (**C**) Comparison of hVASP WT with H89 treated hVASP WT protein interaction network for proteins displayed from panel B. (Red, increase; blue, decrease). (**D**) Bar plot of Gene Ontology analysis of proteins differentially purified from hVASP expressing apoE4 Neuro-2a cells in the absence or presence of H89. Proteins in Gene ontology analysis using EnrichR were determined by a $p < 0.05$ and a $\log_2$ fold change >1 and sorted with p-value ranking. (**E**) Localization of VASP in apoE4 Neuro-2a cells in the absence or presence of 10μM H89 for 24h. Phalloidin staining is for F-actin. DAPI: Nuclear staining. The scale bar is 10μm.

To prioritize PPIs dependence on hVASP S239 phosphorylation status, we filtered the APMS data for proteins with differential binding (>2-fold) between WT hVASP and S239A hVASP, as well as differential binding upon dephosphorylation of WT S239 by H89 treatment. Additionally, to control for H89 effects on hVASP PPIs that may not be related to its S239 phosphorylation status, we further filtered PPIs to those that were relatively unchanged (<2-fold) in S239A mutant cells upon H89 treatment. These criteria resulted in a set of 29 proteins

whose interactions were consistent across all conditions except when hVASP was in a highly phosphorylated state at position S239 (i.e. WT) (**Fig. 4B, Table S3**). Blocking hVASP S239 phosphorylation increased PPIs with components of the actin cytoskeleton (**Fig. 4C**). For instance, hVASP interactions with microfilament motor activity proteins Myo1b, Myo1c, and Myo5a were increased following PKA inhibition in apoE4 Neuro-2a cells. Myo1b is involved in neurite outgrowth, cell migration, axon formation, and growth cone dynamics (Iuliano et al., 2018). Actin nucleating and branching protein Arp2/3 and its component Actr3, as well as Actin protein Actg1, also preferentially interacted with hVASP upon S239 dephosphorylation by H89 (**Fig. 4C**). In line with this, GO analysis of changes in this protein interaction network showed an enrichment of pathways associated with actin filament transport, trafficking, and reorganization (**Fig. 4D**).

We next asked whether the observed changes in PPIs were influenced by VASP subcellular localization in apoE4 Neuro-2a cells, comparing VASP and F-actin subcellular localization patterns in apoE4 Neuro-2a cells in the absence or presence of H89 (**Fig. 4E**). When VASP S235 was phosphorylated, it was predominantly localized at the leading edge and in the cytosol (**Fig 4E**). However upon dephosphorylation of S235 by H89 treatment, VASP became less cytosolic and was enriched as clusters in F-actin containing neurites (**Fig. 4E**). Taken together with APMS data, these findings suggest VASP phosphorylation at S235 by PKA alters actin cytoskeleton protein interactions and subsequently VASP subcellular localization in apoE4 Neuro-2a cells.

Inhibition of PKA promotes filopodia formation and neurite outgrowth in apoE4 cells. Previous studies have shown that apoE4 expression inhibits neurite outgrowth (Nathan et al., 1994, 1995), a process which is initiated by robust filopodia formation (Dent et al., 2007). The observation of long F-actin neurite structures upon PKA inhibition in apoE4 Neuro-2a cells led us to hypothesize that VASP S235 phosphorylation could be an apoE allele-specific mechanism regulating neurite outgrowth and synaptic remodeling through actin cytoskeleton-dependent processes. To test this, we used H89 to inhibit VASP S235 phosphorylation in both apoE3 and apoE4 Neuro-2a cells, and quantified the impact on filopodia formation and neurite outgrowth. As expected, under normal conditions, apoE4 cells had moderately shorter filopodia than apoE3 cells. However, PKA inhibition resulted in a dramatic increase in the length of filopodia in apoE4 cells, some of which appeared to form neurites (**Fig. 5A,C**). Next, we measured neurite outgrowth under these same conditions and observed that indeed, neurite outgrowth was significantly increased in H89-treated apoE4 cells as compared to control apoE4 cells (**Fig. 5B,D**). In contrast, H89 treatment cells did not significantly increase neurite outgrowth in apoE3 cells. Taken together, these results show that in apoE4 cells, depletion of VASP S235 phosphorylation by inhibition of PKA leads to extended filopodia length and subsequently neurite outgrowth.

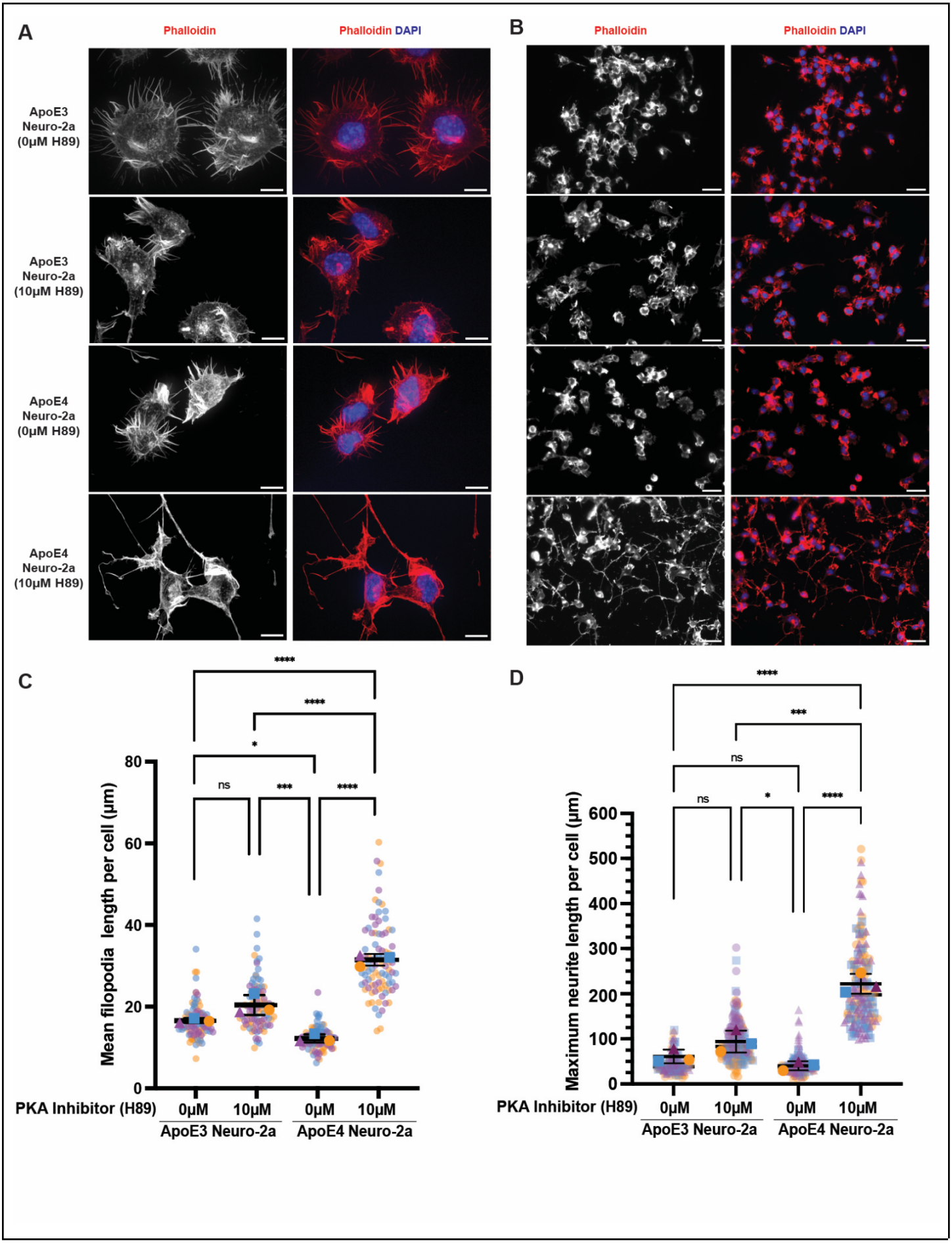
A
Phalloidin
Phalloidin DAPI
ApoE3 Neuro-2a (0μM H89)
ApoE3 Neuro-2a (10μM H89)
ApoE4 Neuro-2a (0μM H89)
ApoE4 Neuro-2a (10μM H89)
B
Phalloidin
Phalloidin DAPI
C
Mean filopodia length per cell (μm)
0
20
40
60
80
****
****
*
ns
***
****
PKA Inhibitor (H89)
0μM
10μM
0μM
10μM
ApoE3 Neuro-2a
ApoE4 Neuro-2a
D
Maximum neurite length per cell (μm)
0
100
200
300
400
500
600
****
***
ns
ns
*
****
PKA Inhibitor (H89)
0μM
10μM
0μM
10μM
ApoE3 Neuro-2a
ApoE4 Neuro-2a

Figure 5. PKA inhibition increases filopodia and neurite length. (**A-B**) Phalloidin staining of apoE3 or apoE4 expressing Neuro-2a cells in the absence or presence of 10μM PKA inhibitor (H89), DAPI: Nuclear staining. Images in panel B are lower magnification to show more cells; scale bar is 10μm (A) and 200μm (B). (**C-D**) Measurement of mean of filopodia and max neurite length per cell using NeuronJ (Meijering et al., 2004). Data represents n=3 independent samples (biological replicates). Each small data point (purple, blue, yellow) represents the length per cell, color-coded by the sample; error bars are ±s.d. of the biological replicates. The triangle represents the average of purple data points, the square represents the average of blue data points, the sphere represents the average of yellow data points. *P* values were calculated using the means of the biological replicates (ns: non significant, * $p<0.05$; *** $p<0.001$; **** $p<0.0001$; with one-way ANOVA analysis with Tukey's multiple comparison test).

Discussion.

Neurons can undergo dramatic morphological changes, forming abundant neurite extensions, axonal elongations, synaptic spines and synapses, all guided by cytoskeletal elements. Disruptions to these cytoskeletal processes are a common feature of AD neuropathogenesis, leading to abnormal actin-containing inclusions, NFT formation and synaptic deficits (Bamburg and Bloom, 2009). These phenotypes can be specifically regulated by apoE4 expression, which has been documented to result in cytoskeletal impairments via mechanisms that have remained unclear (Bellosta et al., 1995; Brodbeck et al., 2011; Chen et al., 2012; Nathan et al., 1994, 1995). The global phosphoproteomics analysis presented here provides insights into the molecular mechanisms of this process, implicating PKA and the actin-interacting protein VASP.

Our findings demonstrate that apoE4 expression results in differential phosphorylation of > 1000 peptides, resulting in rewiring of the phosphorylation signaling architecture to increase PKA activity. Our observations in Neuro-2a cells are supported by clinical data, in which phosphorylation signaling was found to readily distinguish AD patients from other conditions, including progressive supranuclear palsy (PSP), mild cognitive impairment, or individuals with high pathology but low cognitive impact (Bai et al., 2020). Additionally, several phosphoproteomics studies have demonstrated that PKA activity is up-regulated in AD patient brains (Bai et al., 2020; Morshed et al.). Unfortunately, due to technical limitations, phosphorylation of human VASP at S239 has only been detected in a handful of apoE3/4 cases (Morshed et al.), thus further studies will be required to evaluate if this phosphorylation site is correlated with apoE4 allele status, AD diagnosis, or cytoskeletal dysfunction in patients.

Previous work has established a role for apoE4 in promoting PKA activity. For example, in smooth muscle cells and mouse embryonic fibroblasts, extracellular apoE4 can bind to LRP1, resulting in increased cAMP levels and consequently activation of PKA (Zhu and Hui, 2003). Internalization of apoE4 through the LRP receptor has been shown to reduce neurite extension and branching in Neuro-2a cells (Bellosta et al., 1995). Furthermore, incubation of rat primary hippocampal neurons with extracellular apoE4 results in the stimulation of the cAMP response element-binding protein (CREB) (Ohkubo et al., 2001), a downstream PKA target. Our results build upon these observations, and indicate that of the many potential downstream PKA targets, VASP S235 phosphorylation is dramatically upregulated in the apoE4-expressing cells.

We found that PKA inhibition increased the interaction of VASP with proteins such as Myo1b, Myo5a, Tmod2 and Tmod3, which are involved in actin filament organization, vesicle transport along the actin filaments and actomyosin structure organization. This suggests that apoE4-dependent cytoskeletal dysfunction through VASP phosphorylation at S235 could be reversed by PKA inhibition. There is evidence that in response to an increase in cAMP levels in neurons, PKA subunit C translocates from the cytosol to the plasma membrane to phosphorylate its substrates (Tillo et al., 2017). As VASP is localized at the leading edge, phosphorylation of S235 by PKA may prevent VASP from being involved in filopodia formation and neurite initiation.

Filopodia are composed of VASP clusters, parallel filament actin bundles, and other actin binding proteins such as lamellipodin (Drees and Gertler, 2008). Together with microtubules, filopodia are required for neurite initiation and axon extension, which are essential processes for neuronal migration, synapse formation and axon outgrowth and guidance (Drees and Gertler, 2008; Kwiatkowski et al., 2007; Lin et al., 2007; Sarojini and Chakko, 1975). Accordingly, our abundance and phosphoproteomics data suggest that numerous proteins involved in actin cytoskeleton organization, actin filament-based processes, cell leading edge, postsynaptic

actin cytoskeleton organization and microtubule-based transportation are reduced in apoE4 Neuro-2a cells. In contrast, proteins involved in actin filament fragmentation, actin filament severing and depolymerization processes are elevated in apoE4 Neuro-2a cells. Surprisingly, in contrast to our findings, previous studies have shown that neurite initiation and length are reduced upon PKA inhibition in zebrafish neurons and rat hippocampal neurons (Guo et al., 2021; Kao et al., 2002), however these studies did not evaluate the impact of apoE4 on these phenotypes.

In summary, our results suggest a mechanism where increased PKA activity and VASP S235 phosphorylation may limit cytoskeletal dynamics in apoE4 neurons, and consequently limit the capacity for such neurons to engage in synaptic remodeling. Importantly, our results also indicate that this phenotype can be reversed upon PKA inhibition. Thus, further elucidation of the role of PKA in actin cytoskeleton reorganization may lead to novel intervention strategies critical for apoE4-dependent neuropathologies.

Acknowledgements. We thank Yadong Huang, Kristen Skruber, Anke Meyer-Franke, and Michael McGregor for helpful discussions. This work was supported by an NIH grant R01AG059751 to RWM, NJK, and DLS, an NIH grant R35GM118119 to RDM, and funding from the Howard Hughes Medical Institute Investigator Program to RDM.

Conflicts of interest. The NJK laboratory has received research support from Vir Biotechnology and F. Hoffmann-La Roche. NJK has consulting agreements with the Icahn School of Medicine at Mount Sinai, New York, Maze Therapeutics and Interline Therapeutics, is a shareholder of Tenaya Therapeutics and has received stocks from Maze Therapeutics and Interline Therapeutics. DLS has a consulting agreement with Maze Therapeutics. RWM is the co-founder and shareholder of Escape Bio, Inc. RWM is the CEO, CSO, and shareholder of the stem cell company GABAeron, Inc.

Data availability. Mass spectrometry data files (raw and search results) have been deposited to the ProteomeXchange Consortium (http://proteomecentral.proteomexchange.org) via the PRIDE partner repository with dataset identifier PXD034346 (user name: reviewer_pxd034346@ebi.ac.uk, password: 8g9e29n4) (Vizcaíno et al., 2016).

Author contributions.

Zeynep Cakir: Conceptualizing, investigation, visualization, validation, formal analysis, writing-original draft, writing - reviewing & editing. **Samuel J. Lord:** Investigation, Visualization, Resources. **David Jimenez-Morales:** Formal analysis. **Gwendolyn M. Jang:** Investigation. **Benjamin J. Polacco:** Formal analysis and visualization. **Manon Eckhardt:** Writing - Review & Editing. **Billy W. Newton:** Investigation. **Yuan Zhou:** Formal analysis and visualization. **Adam L. Orr:** Investigation. **Jeffery R. Johnson:** Methodology, investigation, software, supervision. **R. Dyche Mullins:** Resources. **Nevan J. Krogan:** Conceptualization, supervision, and funding acquisition. **Robert W. Mahley:** Conceptualization, resources, writing - reviewing & editing, supervision, project administration, and funding acquisition. **Danielle L. Swaney:** Conceptualization, methodology, resources, writing - original draft, writing - reviewing & editing, visualization, supervision, project administration, and funding acquisition.

Supplementary figures

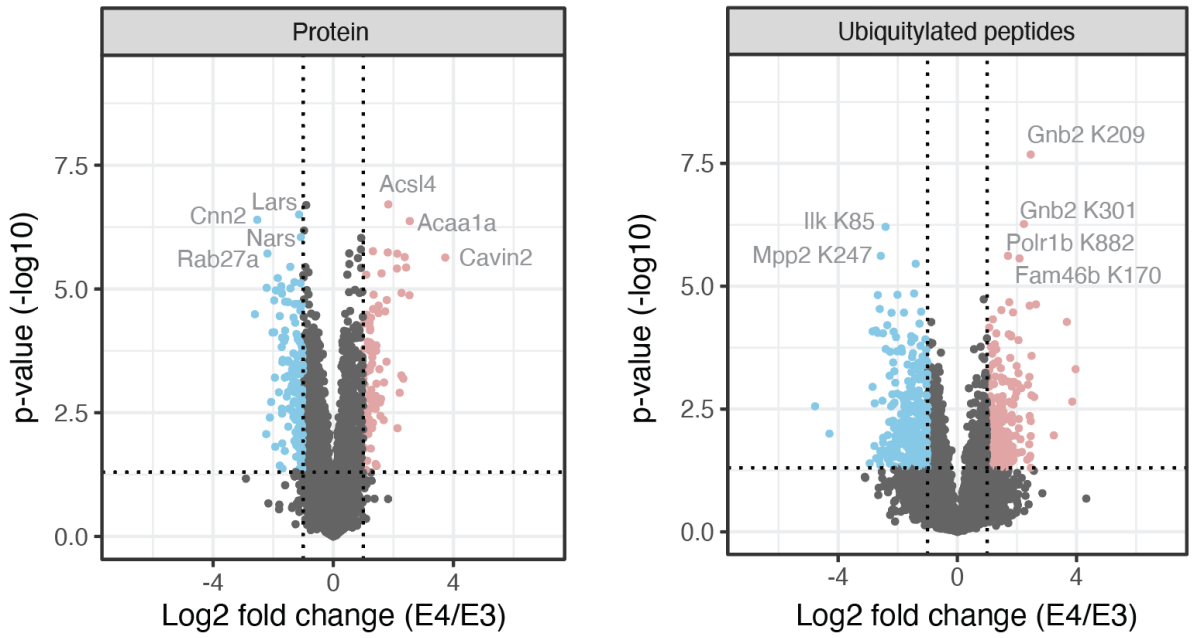

Fig S1. Volcano plots for quantified proteins and ubiquitylation sites. Colored data points indicate analytes with $p < 0.05$ and a $|\log_2$ fold change $> 1|$. A selection of significantly regulated proteins are annotated with their gene names and a selection of ubiquitylated peptides are annotated with their gene name and the modified amino acid position.

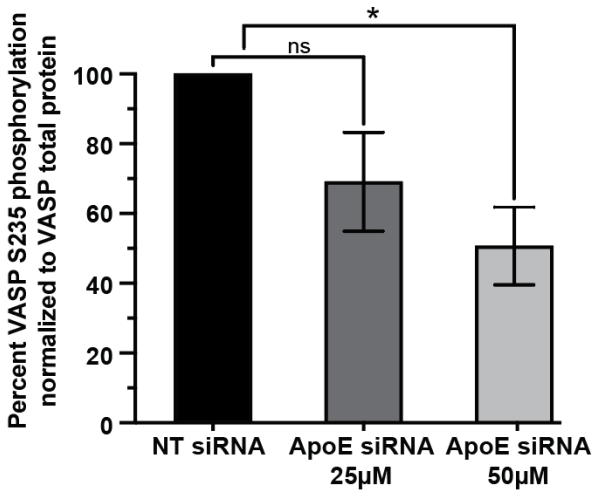

Figure S2. Quantification of VASP S235 phosphorylation levels upon apoE siRNA knockdown. Values are normalized to VASP protein levels, (n=2 biological replicates), ns:non significant, *: p<0.05.

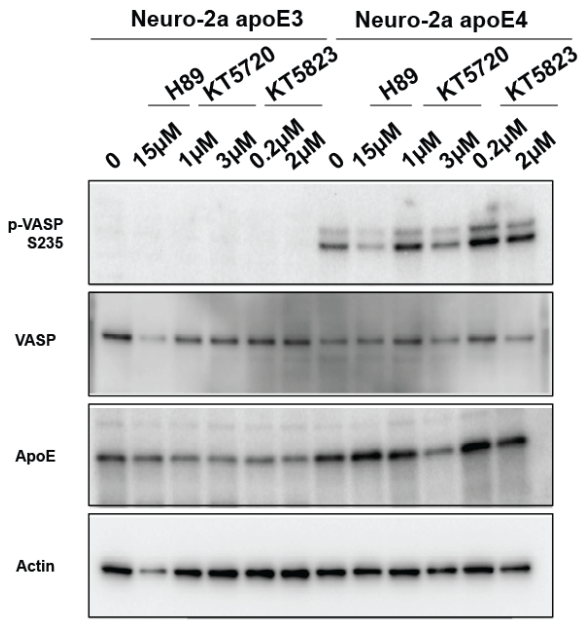

Figure S3. VASP S235 phosphorylation levels in apoE3 Neuro-2a and apoE4 Neuro-2a cells are determined by immunoblotting following treatment with PKA (KT5720) (1μM and 3μM) or PKG (KT5823) inhibitors. Cells were treated either with 1μM and 3μM of KT5720 or 0.2μM and 2μM of KT5823 for 24h.

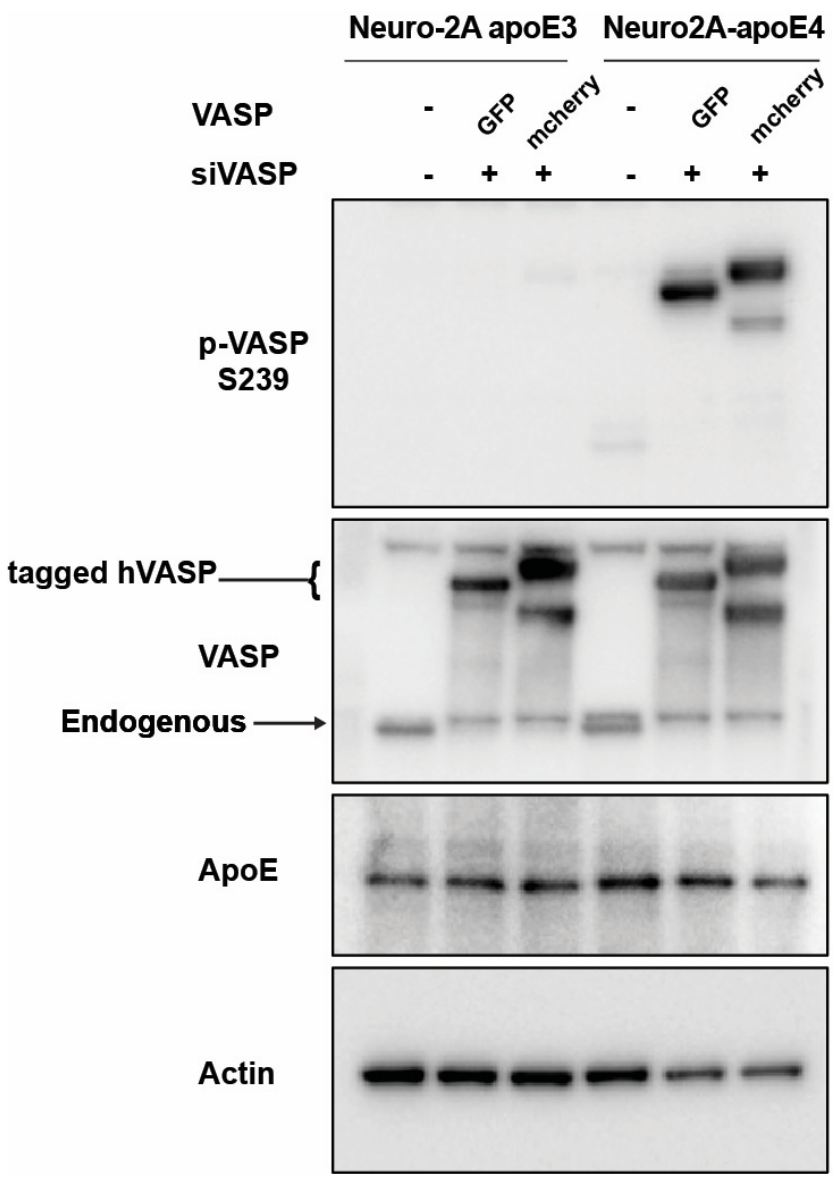

Figure S4. GFP and mcherry-tagged hVASP constructs were expressed in apoE3 and apoE4 Neuro-2a cells for 24h. Endogenous VASP was knocked down by VASPsiRNA. hVASP phosphorylation at S239 was validated by immunoblotting. Endogenous VASP is shown with arrows and hVASP is shown as tagged in brackets. Actin serves a loading control.

Methods.

Cell culture. Mouse neuroblastoma Neuro-2a cell lines stably expressing full-length human apoE3 or apoE4 have been described previously (Harris et al., 2004). Cells were cultured in MEM medium containing 1x glutamax (Cat.#41090036, Gibco), 10% fetal bovine serum (Cat.#A3160402, Gibco), 1% nonessential amino acids (Cat.#11140050, Gibco), 1 mM sodium pyruvate (Cat.#11360-070, Gibco).

Cell lysis and digestion. Nearly confluent Neuro-2a apoE3 or apoE4 cells growing on 15cm dishes were rinsed once with 10 mL of ice-cold 1x PBS and scraped off the plate in 10 mL fresh ice-cold 1x PBS. Cells were pelleted at 4°C for 10 min at 1,500 rpm, the supernatant was decanted, and cells rinsed by resuspending in 10 mL fresh ice cold 1x PBS and pelleting again at 4°C for 10 min at 1,500 rpm. Finally, cells were flash

frozen on dry ice and stored at –80°C until all replicates were collected. Three independent sets of cultures were harvested separately.

Cells were lysed by probe sonication on ice in a buffer composed of 8 M urea, 100 mM ammonium bicarbonate pH 8.0, 150 mM NaCl, and cOmplete mini protease (Cat.#1183615300, Roche) and phosphatase inhibitors (PHOSS-RO, Roche). Proteins were reduced by the addition of 4 mM TCEP and incubated at 22°C for 30 min. Cysteines were alkylated by the addition of 10 mM iodoacetamide and lysates were incubated in the dark at 22°C for 30 min. Alkylation was quenched by the addition of 10 mM DTT and lysates were further incubated in the dark at 22°C for 30 min. Next, proteins were digested overnight at 37°C by the addition of trypsin (Promega) at a 1:100 enzyme:substrate ratio. Samples were acidified to pH 2 with trifluoroacetic acid and desalted on C18 SepPak cartridges (Waters).

Phosphopeptide enrichment. Immobilized metal affinity chromatography (IMAC) beads for phosphopeptide enrichment were prepared by stripping Ni-NTA Superflow beads (Qiagen) with 100 mM EDTA (pH 7.5), followed by loading of the beads with iron by incubated in 15 mM ferric chloride solution. The beads were then washed with water and then 15uL of beads were loaded into the top of a C18 microspin column. Approximately 1mg of desalted peptides was resuspended in 75% acetonitrile, 0.15% trifluoroacetic acid, and loaded onto IMAC tips by pipetting and incubated for 4 min, with intermittent mixing by pipetting. The lysate was then passed through the column, followed by 4 washes with 200 µL of 80% acetonitrile, 0.1% trifluoroacetic acid. The column was then equilibrated twice for 2 min with 200 µL of 0.5% formic acid, with intermittent mixing by pipetting. Next, the bound phosphorylated peptides were eluted from the IMAC beads onto the C18 column by the addition of 200 µL of 500 mM potassium phosphate buffer (pH 7), which was incubated with the beads for 3 min with intermittent mixing by pipetting. The potassium phosphate elution was repeated once, and then the column was equilibrated twice for 15 s with 200 µL of 0.5% formic acid. Finally, the phosphopeptides were eluted from the C18 column twice by the addition of 75 µL of 50% acetonitrile in 0.1% formic acid and the eluted phosphopeptides were dried by vacuum centrifugation.

Ubiquitylated peptide enrichment. Approximately 1/8th of a tube of anti PTMScan Ubiquitin Remnant Motif antibody beads (Cell Signaling Technologies) was used per sample. All steps were performed at 4°C unless otherwise noted. The beads were first washed twice in IAP buffer (50 mM MOPS, 10 mM sodium phosphate buffer (pH 7.2), 50 mM NaCl) and then ~5 mg of desalted peptides that had been resuspended in IAP was added to the beads. The samples were incubated with rotation for 90 min, and then the beads were washed twice with IAP buffer, followed by two washes with water. Next, peptides were eluted from the beads by the addition of 60 µL of 0.15% trifluoroacetic acid to the beads for 10 min with gentle vortexing. The supernatant containing the ubiquitin enriched peptide eluent was then transferred to a new tube, and the elution was repeated by the addition of another 60 µL of 0.15% trifluoroacetic acid. The second elution was combined with the first, and then desalted on C18 columns (The Nest Group), and the desalted peptides were dried by vacuum centrifugation.

Mass spectrometry data acquisition. Peptides were resuspended in 4% formic acid and 3% acetonitrile and directly injected on a 75 µm ID column (New Objective) packed with 25 cm of Reprosil C18 1.9 µm, 120 Å particles (Dr. Maisch) for AB, PH, and UB experiments. For APMS experiments, peptides were resuspended in 0.1% formic and directly injected onto a PepSep column (Bruker) packed with 15 cm of Reprosil C18 1.5 µm, 120 Å particles (Dr. Maisch). Peptides were eluted in positive ion mode into an Orbitrap Fusion Tribrid mass spectrometer (Thermo Fisher Scientific) with an acetonitrile gradient delivered by an Easy1000 nLC system (PH, AB, and UB) or an Easy1200 nLC system (APMS) (Thermo Fisher Scientific). All mobile phases contained 0.1% formic acid as buffer A. For AB and PH experiments the total MS acquisition time was 180 min, during which mobile phase buffer B (0.1% formic acid in 90% acetonitrile) was ramped from 5% to 16% B over 114 min, followed by a ramp to 30% buffer B over a subsequent 50 min, and then a ramp to 95% B to wash the column. For the UB experiment the total MS acquisition time was 120 min, during which mobile phase buffer B (0.1% formic acid in 90% acetonitrile) was ramped from 5% to 33% B over 105 min, followed by a ramp to 100% B to wash the column. For APMS experiments, the total MS acquisition time was 60 min, during which mobile phase buffer B (0.1% formic acid in 80% acetonitrile) was ramped from 3% to 28% B over

44 min, followed by a ramp to 45% B over a subsequent 5 minutes, and lastly a ramp to 88% B to wash the column.

For AB, PH, and UB experiments data was collected on an Orbitrap Fusion Tribrid Mass Spectrometer (Thermo Fisher Scientific). The ion transfer tube was set to 300°C, the spray voltage was 1800-2000V, MS1 scan was collected in the orbtrap in profile mode with 120K resolution over a scan range of 400-1600 m/z, a 100 ms maximum injection time, 2e6 AGC target, S-Lens RF of 60. Charges states 2-7 were considered for MS2 scan selection using MIPS filtering, exclusion of undetermined charge states, a 5e3 minimum signal intensity, and a 20s dynamic exclusion with a +/- 10 ppm window. MS2 scans were performed over the course of a 3s cycle, a 1.6 m/z quadrupole isolation, 29% (UB) or 30% (PH and AB) normalized collision energy, HCD fragmentation, a 110 m/z first mass, ion trap detection with a rapid scan rate, 35ms maximum injection time, 1e4 AGC target, centroid data type, and the allowance to injection ions for all available parallelizable time. For APMS experiments data was collected on an Orbtrap Fusion Lumos Tribrid Mass Spectrometer (Thermo Fisher Scientific). The ion transfer tube was set to 275°C, the spray voltage was 2000V, MS1 scan was collected in the orbitrap in profile mode with 240K resolution over a scan range of 350-1350 m/z, a 50 ms maximum injection time, 1e6 AGC target, S-Lens RF of 30. Charges states 2-5 were considered for MS2 scan selection using MIPS filtering, advance peak determination, exclusion of undetermined charge states, a 5e3 minimum signal intensity, and a 20s dynamic exclusion with a +/- 10 ppm window in which 2 occurrences were allowed. MS2 scans were performed over the course of a 1s cycle, a 0.7 m/z quadrupole isolation, 32% normalized collision energy, HCD fragmentation, a 200-1200 m/z scan range, ion trap detection with a rapid scan rate, 18ms maximum injection time, 3e4 AGC target, centroid data type.

Proteomics data analysis. All data were searched against the *Mus musculus* UniProt database canonical sequences. Additionally, APMS data was searched against the human apoE3 and apoE4 sequences, as well as the Raph1 mouse sequence. Peptide and protein identification searches, as well as label-free quantitation were performed using the MaxQuant data analysis algorithm (Cox and Mann, 2008), and all peptide, protein, and modification site identifications were filtered to a 1% false-discovery rate. Default MaxQuant settings were used, with the exception that match between runs was enabled with a window of 2 min (PH and AB), 1 min (UB), or 0.7 min (APMS) for each data type respectively. Additionally, for phosphorylation data a variable phosphorylation modification was considered on STY residues, while for ubiquitylation data a variable modification of di-glycine was considered on all K residues. Mass spectrometry data files (raw and search results) have been deposited to the ProteomeXchange Consortium (http://proteomecentral.proteomexchange.org) via the PRIDE partner repository with dataset identifier PXD034346 (user name: reviewer_pxd034346@ebi.ac.uk, password: 8g9e29n4) (Vizcaíno et al., 2016).

Label-free quantification and statistical analysis for both global proteomics and APMS data was performed using MSstats (Choi et al., 2014). Note, for consistent statistical testing across global proteomics data types, the previously published protein abundance analysis (Orr et al., 2019) was re-analyzed using a more recent version of the MSstats R-package (version 3.3.10), such that this same MSstats version was used for all global proteomics data types reported here. Enrichment analysis was performed using the enricher function from R packages clusterProfiler (version 3.99.0) (Yu et al., 2012). The gene ontology terms and annotations were obtained from the R annotation package org.Mm.eg.db (version 3.12.0). We selected the most significant GO term from among redundant GO terms, which were identified using a hierarchical tree based on distances (1-Jaccard Similarity Coefficients of shared genes in GO) between the significant terms, and then cut the tree into clusters containing redundant terms (R functions hclust and cutree, cut height = 0.99). A ranked list of protein abundance values was used to perform tissue type enrichment using the “Protein with Values/Ranks" function in STRING (Szklarczyk et al., 2021). For APMS experiments, interacting protein abundance values derived from MSstats (Choi et al., 2014) were visualized using Morpheus (https://software.broadinstitute.org/morpheus) and VASP differential protein-protein interaction networks were visualized in Cytoscape (Shannon et al., 2003) with edges between interacting proteins being supplemented from STRING (Szklarczyk et al., 2021).

siRNA knockdowns. Pre-designed silencer select siRNAs against APOE, VASP and negative control were ordered from ThermoFisher (Cat.#160728, Cat.#AM16708, Cat.#AM461, respectively). ApoE3 and apoE4

Neuro-2a cells were transfected with siRNA using Lipofectamine RNAiMax (Cat#13778075, Thermo Scientific). Cells were seeded into 6-well plates and transfection protocol was followed according to manufacturer's instructions (Cat.#13778075, Invitrogen).

Constructs. Human GFP-Vasp and mCherry-VASP was gifted by D. Mullins, University of California, San Francisco. Phospho-null mutation VASP S239A was generated using the QuikChange II Site-Directed Mutagenesis Kit (Cat.#200523, Agilent). Primers were designed using the QuikChange Primer Design Program and obtained from Integrated DNA Technologies IDT. VASP S239A Forward Primer: GGCCTCCTCCTGCTTGGCGACTTTCCTGAGTTTG, VASP S239A Reverse Primer: CAAACTCAGGAAAGTCGCCAAGCAGGAGGAGGCC. GFP-VASP and mCherry-VASP constructs were transfected using Polyjet transfection reagent (Cat.#SL100688, Signagen) following the manufacturer's protocol.

Immunoblotting. Cells were lysed in ice-cold RIPA buffer supplemented with cOmplete mini protease inhibitor cocktail (Cat.#1183615300, Roche) and PhosSTOP (PHOSS-RO, Roche). Protein concentration was measured by a Pierce BCA protein assay kit (Cat.#A329645, Life Technologies) and 20ug protein was loaded on a 4%-12% acrylamide gel (Criterion TGX,Cat.#5671095, Biorad). The samples were separated by sodium dodecyl sulfate polyacrylamide gel electrophoresis (SDS-PAGE) and transferred with PVDF membrane (Trans Blot Turbo, Cat.#1704157, Biorad). Membranes are blocked in %5 Milk with Tris-buffered saline with 0.1% Tween 20 detergent (TBST). Primary antibodies were prepared in 5%BSA-TBST and incubated overnight at 4°C. The membranes were washed in TBST and incubated 2 h in species-specific horseradish peroxidase-conjugated secondary antibodies (1:3000-1:5000). Membranes were visualized using chemiluminescence substrate (Pierce ECL, Cat.#32209,Thermo Scientific) and imaged with ChemiDOC MP (Bio-Rad). Antibodies : VASP S239 1:1000 (ab194747,Abcam), VASP 1:1000 (13472-1-AP, Proteintech) ApoE 1:2000 (178479, EMD Milipore) , Actin 1:1000 (4970L, CST), Akt 1:1000 (9272S, CST), p-AKT T308 1:1000 (13038S, CST), p-AKT S473 1:1000 (4060S, CST).

GFP-VASP Affinity Purification MS. ApoE4 Neuro2a cells were seeded to the 15cm dish. On the day of transfection, cells were transfected with Polyjet using 9ug of GFP-VASP WT and GFP-VASP S239A constructs according to the manufacturer's instructions (Cat.# SL100688, Signagen). After 8h of transfection, cells were treated either with DMSO control or 15μM H89 and cells were collected after 24h of treatment.

Frozen cell pellets were thawed at room temperature and suspended in 0.5 mL Lysis Buffer [IP Buffer (50 mM Tris-HCl, pH 7.4 at 4°C, 150 mM NaCl, 1 mM EDTA) supplemented with 0.5% Nonidet P 40 Substitute (NP40; Fluka Analytical) and cOmplete mini EDTA-free protease and PhosSTOP phosphatase inhibitor cocktails (Roche)]. Cell suspensions were immediately subjected to one freeze-thaw cycle (at least 20 min on dry ice and partial thawing at 37°C) then refrozen and kept at -80°C until immunoprecipitation. Lysis was completed by partially thawing frozen samples at 37°C and incubating on a tube rotator at 4°C for 30 min. After pelleting debris at 13,000 xg, 4°C for 15 minutes, 25 μL lysate was reserved before proceeding (below). A ThermoMixer C incubator was used to thaw samples at indicated temperatures with constant shaking at 1,100 rpm for 1-2 min; otherwise, samples were kept cold.

For each equilibration/wash step (below), GFP-Trap magnetic agarose beads (20 μL in first plate only; Cat.#GTMA-10, Chromotek) and/or up to 1.0 mL buffer were pre-aliquoted into 96 Deep-well plates, while 0.45 mL lysate was arrayed for each sample. All plates were kept on ice until loaded onto the KingFisher Flex (KFF) Purification System (Thermo Scientific) for automated processing as follows: GFP-Trap beads were equilibrated twice with IP Wash Buffer (IP Buffer supplemented with 0.05% NP40) and incubated with cell lysates for 2 hours. Protein-bound beads were washed three times with IP Wash Buffer and then once with IP Buffer before elution. After transferring to 1.5-mL lobind tubes, beads were suspended with 50 μL 0.05% RapiGest in IP Buffer and gently agitated on a vortex mixer at room temperature for 30 min to elute proteins and briefly rinsed in 25 μL IP Buffer to recover residual proteins; both were combined for further processing (below). The KFF is operated in a cold room to maintain a 4°C temperature during immunoprecipitation. Automated protocol steps were performed using the slow mix speed and the following mix times: 30 seconds

for equilibration/wash steps, 2 hours for binding, and 1 minute for final bead release. Three 10 second bead collection times were used before bead transfer to the next plate.

Using a 96 well PCR plate, samples were incubated at 37°C in a thermal cycler or at room temperature in a MixMate incubator with shaking at 1,100 rpm for the following steps: Denaturation and reduction at 37°C for 30 minutes with 2 M urea and 1 mM DTT in 50 mM Tris-HCl pH 8.0, alkylation at room temperature for 45 minutes with 3 mM iodoacetamide and quenching for 10 minutes with 3 mM DTT. Trypsin (0.5 µg/µL; Promega) was added twice (1.0 µL and 0.5 µL) and further incubated at 37°C for 4 hours and then another 2 hours. Peptides were acidified with trifluoroacetic acid (TFA, 0.5% final, pH < 2.0) and desalted at room temperature using a BioPureSPE Mini 96-well plate (20mg PROTO 300 C18; The Nest Group). Briefly, desalting columns were sequentially equilibrated with 100% methanol; 80% acetonitrile (ACN), 0.1% TFA and 2% ACN, 0.1% TFA before passing acidified samples through columns twice and subsequently washed with 2% ACN, 0.1% TFA and 0.1% formic acid (FA). 0.2 - 0.3 mL of buffer was added at each step. Peptides were eluted twice with 50% ACN, 0.1% FA (0.12 mL total, divided) and dried under vacuum centrifugation (CentriVap Concentrator, Labconco). The desalting plate was centrifuged at 2,000 rpm for 2-3 minutes. All buffers were prepared with HPLC or LC-MS grade reagents.

Immunofluorescence. Neuro2a cells were cultured on coverslips. After one PBS wash, cells were fixed in 3.7% paraformaldehyde for 10 min. Then, cells were permeabilized with 0.5% TritonX-100 for 5 min, followed by the addition of 100nM Phalloidin to the cells. Phalloidin staining protocol was followed according to manufacturer's instructions (Cat.#PHDH1, Cytoskeleton Inc). For VASP staining, cells were blocked in 5% normal goat serum (NGS) for 15min at room temperature. VASP antibody (13472-1-AP, Proteintech) was prepared in 5% NGS (diluted in 1:200) and incubated overnight at 4°C. The next day, cells were washed with PBS and incubated with the secondary antibody (diluted in 1:500, 5% NGS) at room temperature for 45min. The coverslips were mounted on glass slides using DAPI Fluoromount-G (Cat.#0100-20, Southernbiotech) and imaged using a Visitech iSIM superresolution module and Hamamatsu Quest camera on a Nikon Eclipse Ti-E with a 100x 1.45NA objective. Images were deconvolved using Microvolution and neurite length was calculated using NeuronJ plugin in Fiji, as previously described (Meijering et al., 2004). NeuronJ traces the neurite by finding two points, one at the start and one at the end and calculating the optimal intensity path. Neurite lengths were quantified using Prism graphpad with three independent biological replicates.

Statistical analysis. A two-tailed t-test was performed when two groups were compared and one-way ANOVA or two-way ANOVA with repeated measures was performed when multiple groups were compared, according to different conditions. Statistical analyses were performed with Prism software (GraphPad Software, Inc.). Differences were considered significant at *$p < 0.05$, **$p < 0.01$ and ***$p < 0.001$ ****$p < 0.0001$. SuperPlots in Figure 5 were generated in GraphPad Prism (Lord et al., 2020).

References.

Atamna, H., and Frey, W.H., 2nd (2007). Mechanisms of mitochondrial dysfunction and energy deficiency in Alzheimer's disease. Mitochondrion *7*, 297–310. .

Bai, B., Wang, X., Li, Y., Chen, P.-C., Yu, K., Dey, K.K., Yarbro, J.M., Han, X., Lutz, B.M., Rao, S., et al. (2020). Deep Multilayer Brain Proteomics Identifies Molecular Networks in Alzheimer's Disease Progression. Neuron *105*, 975–991.e7. .

Bamburg, J.R., and Bloom, G.S. (2009). Cytoskeletal pathologies of Alzheimer disease. Cell Motil. Cytoskeleton *66*, 635–649. .

Bellosta, S., Nathan, B.P., Orth, M., Dong, L.M., Mahley, R.W., and Pitas, R.E. (1995). Stable expression and secretion of apolipoproteins E3 and E4 in mouse neuroblastoma cells produces differential effects on neurite

outgrowth. J. Biol. Chem. *270*, 27063–27071. .

Benz, P.M., Blume, C., Seifert, S., Wilhelm, S., Waschke, J., Schuh, K., Gertler, F., Münzel, T., and Renné, T. (2009). Differential VASP phosphorylation controls remodeling of the actin cytoskeleton. J. Cell Sci. *122*, 3954–3965. .

Biundo, F., Ishiwari, K., Del Prete, D., and D'Adamio, L. (2015). Interaction of ApoE3 and ApoE4 isoforms with an ITM2b/BRI2 mutation linked to the Alzheimer disease-like Danish dementia: Effects on learning and memory. Neurobiol. Learn. Mem. *126*, 18–30. .

Brodbeck, J., McGuire, J., Liu, Z., Meyer-Franke, A., Balestra, M.E., Jeong, D.-E., Pleiss, M., McComas, C., Hess, F., Witter, D., et al. (2011). Structure-dependent impairment of intracellular apolipoprotein E4 trafficking and its detrimental effects are rescued by small-molecule structure correctors. J. Biol. Chem. *286*, 17217–17226. .

Bu, G. (2009). Apolipoprotein E and its receptors in Alzheimer's disease: pathways, pathogenesis and therapy. Nat. Rev. Neurosci. *10*, 333. .

Butt, E., Abel, K., Krieger, M., Palm, D., Hoppe, V., Hoppe, J., and Walter, U. (1994). cAMP-and cGMP-dependent protein kinase phosphorylation sites of the focal adhesion vasodilator-stimulated phosphoprotein (VASP) in vitro and in intact human platelets. J. Biol. Chem. *269*, 14509–14517. .

Chen, H.-K., Liu, Z., Meyer-Franke, A., Brodbeck, J., Miranda, R.D., McGuire, J.G., Pleiss, M.A., Ji, Z.-S., Balestra, M.E., Walker, D.W., et al. (2012). Small molecule structure correctors abolish detrimental effects of apolipoprotein E4 in cultured neurons. J. Biol. Chem. *287*, 5253–5266. .

Choi, M., Chang, C.-Y., Clough, T., Broudy, D., Killeen, T., MacLean, B., and Vitek, O. (2014). MSstats: an R package for statistical analysis of quantitative mass spectrometry-based proteomic experiments. Bioinformatics *30*, 2524–2526. .

Corder, E.H., Saunders, A.M., Strittmatter, W.J., Schmechel, D.E., Gaskell, P.C., Small, G.W., Roses, A.D., Haines, J.L., and Pericak-Vance, M.A. (1993). Gene dose of apolipoprotein E type 4 allele and the risk of Alzheimer's disease in late onset families. Science *261*, 921–923. .

Cox, J., and Mann, M. (2008). MaxQuant enables high peptide identification rates, individualized p.p.b.-range mass accuracies and proteome-wide protein quantification. Nat. Biotechnol. *26*, 1367–1372. .

Dent, E.W., Kwiatkowski, A.V., Mebane, L.M., Philippar, U., Barzik, M., Rubinson, D.A., Gupton, S., Van Veen, J.E., Furman, C., Zhang, J., et al. (2007). Filopodia are required for cortical neurite initiation. Nat. Cell Biol. *9*, 1347–1359. .

Domingues, C., Geraldo, A.M., Anjo, S.I., Matos, A., Almeida, C., Caramelo, I., Lopes-da-Silva, J.A., Paiva, A., Carvalho, J., Pires das Neves, R., et al. (2020). Cofilin-1 Is a Mechanosensitive Regulator of Transcription. Front Cell Dev Biol *8*, 678. .

Döppler, H., and Storz, P. (2013). Regulation of VASP by phosphorylation: consequences for cell migration. Cell Adh. Migr. *7*, 482–486. .

Drees, F., and Gertler, F.B. (2008). Ena/VASP: proteins at the tip of the nervous system. Curr. Opin. Neurobiol. *18*, 53–59. .

Farrer, L.A., Adrienne Cupples, L., Haines, J.L., Hyman, B., Kukull, W.A., Mayeux, R., Myers, R.H., Pericak-Vance, M.A., Risch, N., and van Duijn, C.M. (1997). Effects of Age, Sex, and Ethnicity on the Association Between Apolipoprotein E Genotype and Alzheimer Disease: A Meta-analysis. JAMA *278*, 1349–1356. .

Ferron, F., Rebowski, G., Lee, S.H., and Dominguez, R. (2007). Structural basis for the recruitment of profilin-actin complexes during filament elongation by Ena/VASP. EMBO J. *26*, 4597–4606. .

Flynn, K.C., Pak, C.W., Shaw, A.E., Bradke, F., and Bamburg, J.R. (2009). Growth cone-like waves transport actin and promote axonogenesis and neurite branching. Dev. Neurobiol. *69*, 761–779. .

Genin, E., Hannequin, D., Wallon, D., Sleegers, K., Hiltunen, M., Combarros, O., Bullido, M.J., Engelborghs, S., De Deyn, P., Berr, C., et al. (2011). APOE and Alzheimer disease: a major gene with semi-dominant inheritance. Mol. Psychiatry *16*, 903–907. .

Gomez, T.M., Roche, F.K., and Letourneau, P.C. (1996). Chick sensory neuronal growth cones distinguish fibronectin from laminin by making substratum contacts that resemble focal contacts. J. Neurobiol. *29*, 18–34. .

Guo, B., Qi, M., Huang, S., Zhuo, R., Zhang, W., Zhang, Y., Xu, M., Liu, M., Guan, T., and Liu, Y. (2021). Cadherin-12 Regulates Neurite Outgrowth Through the PKA/Rac1/Cdc42 Pathway in Cortical Neurons. Front Cell Dev Biol *9*, 768970. .

Harigaya, Y., Shoji, M., Shirao, T., and Hirai, S. (1996). Disappearance of actin-binding protein, drebrin, from hippocampal synapses in Alzheimer's disease. J. Neurosci. Res. *43*, 87–92. .

Harris, F.M., Brecht, W.J., Xu, Q., Tesseur, I., Kekonius, L., Wyss-Coray, T., Fish, J.D., Masliah, E., Hopkins, P.C., Scearce-Levie, K., et al. (2003). Carboxyl-terminal-truncated apolipoprotein E4 causes Alzheimer's disease-like neurodegeneration and behavioral deficits in transgenic mice. Proc. Natl. Acad. Sci. U. S. A. *100*, 10966–10971. .

Harris, F.M., Brecht, W.J., Xu, Q., Mahley, R.W., and Huang, Y. (2004). Increased tau phosphorylation in apolipoprotein E4 transgenic mice is associated with activation of extracellular signal-regulated kinase: modulation by zinc. J. Biol. Chem. *279*, 44795–44801.

Hoffman, L.M., Jensen, C.C., Kloeker, S., Wang, C.-L.A., Yoshigi, M., and Beckerle, M.C. (2006). Genetic ablation of zyxin causes Mena/VASP mislocalization, increased motility, and deficits in actin remodeling. J. Cell Biol. *172*, 771–782. .

Holtzman, D.M., Herz, J., and Bu, G. (2012). Apolipoprotein E and apolipoprotein E receptors: normal biology and roles in Alzheimer disease. Cold Spring Harb. Perspect. Med. *2*, a006312. .

Huang, Y., and Mucke, L. (2012). Alzheimer mechanisms and therapeutic strategies. Cell *148*, 1204–1222. .

Huang, Y., Liu, X.Q., Wyss-Coray, T., Brecht, W.J., Sanan, D.A., and Mahley, R.W. (2001). Apolipoprotein E fragments present in Alzheimer's disease brains induce neurofibrillary tangle-like intracellular inclusions in neurons. Proc. Natl. Acad. Sci. U. S. A. *98*, 8838–8843. .

Iuliano, O., Yoshimura, A., Prospéri, M.-T., Martin, R., Knölker, H.-J., and Coudrier, E. (2018). Myosin 1b promotes axon formation by regulating actin wave propagation and growth cone dynamics. J. Cell Biol. *217*, 2033–2046. .

James, R., Searcy, J.L., Le Bihan, T., Martin, S.F., Gliddon, C.M., Povey, J., Deighton, R.F., Kerr, L.E., McCulloch, J., and Horsburgh, K. (2012). Proteomic analysis of mitochondria in APOE transgenic mice and in response to an ischemic challenge. J. Cereb. Blood Flow Metab. *32*, 164–176. .

Kao, H.-T., Song, H.-J., Porton, B., Ming, G.-L., Hoh, J., Abraham, M., Czernik, A.J., Pieribone, V.A., Poo, M.-M., and Greengard, P. (2002). A protein kinase A-dependent molecular switch in synapsins regulates neurite outgrowth. Nat. Neurosci. *5*, 431–437. .

Kim, J., Basak, J.M., and Holtzman, D.M. (2009). The role of apolipoprotein E in Alzheimer's disease. Neuron

63, 287–303. .

Knoferle, J., Yoon, S.Y., Walker, D., Leung, L., Gillespie, A.K., Tong, L.M., Bien-Ly, N., and Huang, Y. (2014). Apolipoprotein E4 produced in GABAergic interneurons causes learning and memory deficits in mice. J. Neurosci. *34*, 14069–14078. .

Koutsodendris, N., Nelson, M.R., Rao, A., and Huang, Y. (2021). Apolipoprotein E and Alzheimer's Disease: Findings, Hypotheses, and Potential Mechanisms. Annu. Rev. Pathol. https://doi.org/10.1146/annurev-pathmechdis-030421-112756.

Kwiatkowski, A.V., Gertler, F.B., and Loureiro, J.J. (2003). Function and regulation of Ena/VASP proteins. Trends Cell Biol. *13*, 386–392. .

Kwiatkowski, A.V., Rubinson, D.A., Dent, E.W., Edward van Veen, J., Leslie, J.D., Zhang, J., Mebane, L.M., Philippar, U., Pinheiro, E.M., Burds, A.A., et al. (2007). Ena/VASP Is Required for neuritogenesis in the developing cortex. Neuron *56*, 441–455. .

Lee, V., and Maguire, J. (2014). The impact of tonic GABAA receptor-mediated inhibition on neuronal excitability varies across brain region and cell type. Front. Neural Circuits *8*, 3. .

Legerstee, K., Geverts, B., Slotman, J.A., and Houtsmuller, A.B. (2019). Dynamics and distribution of paxillin, vinculin, zyxin and VASP depend on focal adhesion location and orientation. Sci. Rep. *9*, 10460. .

Lin, Y.-L., Lei, Y.-T., Hong, C.-J., and Hsueh, Y.-P. (2007). Syndecan-2 induces filopodia and dendritic spine formation via the neurofibromin-PKA-Ena/VASP pathway. J. Cell Biol. *177*, 829–841. .

Liu, C.-C., Liu, C.-C., Kanekiyo, T., Xu, H., and Bu, G. (2013). Apolipoprotein E and Alzheimer disease: risk, mechanisms and therapy. Nat. Rev. Neurol. *9*, 106–118. .

Lord, S.J., Velle, K.B., Mullins, R.D., and Fritz-Laylin, L.K. (2020). SuperPlots: Communicating reproducibility and variability in cell biology. J. Cell Biol. *219*. https://doi.org/10.1083/jcb.202001064.

Lucas, E.K., and Clem, R.L. (2018). GABAergic interneurons: The orchestra or the conductor in fear learning and memory? Brain Res. Bull. *141*, 13–19. .

Luo, S., Schaefer, A.M., Dour, S., and Nonet, M.L. (2014). The conserved LIM domain-containing focal adhesion protein ZYX-1 regulates synapse maintenance in Caenorhabditis elegans. Development *141*, 3922–3933. .

Mahley, R.W. (1988). Apolipoprotein E: cholesterol transport protein with expanding role in cell biology. Science *240*, 622–630. .

Mahley, R.W., and Huang, Y. (2012a). Apolipoprotein e sets the stage: response to injury triggers neuropathology. Neuron *76*, 871–885. .

Mahley, R.W., and Huang, Y. (2012b). Small-molecule structure correctors target abnormal protein structure and function: structure corrector rescue of apolipoprotein E4-associated neuropathology. J. Med. Chem. *55*, 8997–9008. .

Mahley, R.W., Weisgraber, K.H., and Huang, Y. (2006). Apolipoprotein E4: a causative factor and therapeutic target in neuropathology, including Alzheimer's disease. Proc. Natl. Acad. Sci. U. S. A. *103*, 5644–5651. .

Mahley, R.W., Weisgraber, K.H., and Huang, Y. (2009). Apolipoprotein E: structure determines function, from atherosclerosis to Alzheimer's disease to AIDS. J. Lipid Res. *50 Suppl*, S183–S188. .

Martens, Y.A., Zhao, N., Liu, C.-C., Kanekiyo, T., Yang, A.J., Goate, A.M., Holtzman, D.M., and Bu, G. (2022). ApoE Cascade Hypothesis in the pathogenesis of Alzheimer's disease and related dementias. Neuron

https://doi.org/10.1016/j.neuron.2022.03.004.

Meijering, E., Jacob, M., Sarria, J.-C.F., Steiner, P., Hirling, H., and Unser, M. (2004). Design and validation of a tool for neurite tracing and analysis in fluorescence microscopy images. Cytometry A *58*, 167–176. .

Morshed, N., Lee, M., Rodriguez, F.H., Lauffenburger, D.A., Mastroeni, D., and White, F. Quantitative phosphoproteomics uncovers dysregulated kinase networks in Alzheimer's disease. https://doi.org/10.1101/2020.08.18.255778.

Nathan, B.P., Bellosta, S., Sanan, D.A., Weisgraber, K.H., Mahley, R.W., and Pitas, R.E. (1994). Differential effects of apolipoproteins E3 and E4 on neuronal growth in vitro. Science *264*, 850–852. .

Nathan, B.P., Chang, K.C., Bellosta, S., Brisch, E., Ge, N., Mahley, R.W., and Pitas, R.E. (1995). The inhibitory effect of apolipoprotein E4 on neurite outgrowth is associated with microtubule depolymerization. J. Biol. Chem. *270*, 19791–19799. .

Ohkubo, N., Mitsuda, N., Tamatani, M., Yamaguchi, A., Lee, Y.D., Ogihara, T., Vitek, M.P., and Tohyama, M. (2001). Apolipoprotein E4 stimulates cAMP response element-binding protein transcriptional activity through the extracellular signal-regulated kinase pathway. J. Biol. Chem. *276*, 3046–3053. .

Orr, A.L., Kim, C., Jimenez-Morales, D., Newton, B.W., Johnson, J.R., Krogan, N.J., Swaney, D.L., and Mahley, R.W. (2019). Neuronal Apolipoprotein E4 Expression Results in Proteome-Wide Alterations and Compromises Bioenergetic Capacity by Disrupting Mitochondrial Function. J. Alzheimers. Dis. *68*, 991–1011. .

Parihar, M.S., and Brewer, G.J. (2007). Mitoenergetic failure in Alzheimer disease. Am. J. Physiol. Cell Physiol. *292*, C8–C23. .

Reinhard, M., Jarchau, T., and Walter, U. (2001). Actin-based motility: stop and go with Ena/VASP proteins. Trends Biochem. Sci. *26*, 243–249. .

Sarojini, S., and Chakko, T.V. (1975). Activity of neurosecretory cells in relation to ovarian cycle of the viviparous cockroach, Nauphoeta cinerea (Olivier). Indian J. Exp. Biol. *13*, 196–199. .

Shannon, P., Markiel, A., Ozier, O., Baliga, N.S., Wang, J.T., Ramage, D., Amin, N., Schwikowski, B., and Ideker, T. (2003). Cytoscape: a software environment for integrated models of biomolecular interaction networks. Genome Res. *13*, 2498–2504. .

Shi, L., Du, X., Zhou, H., Tao, C., Liu, Y., Meng, F., Wu, G., Xiong, Y., Xia, C., Wang, Y., et al. (2014). Cumulative effects of the ApoE genotype and gender on the synaptic proteome and oxidative stress in the mouse brain. Int. J. Neuropsychopharmacol. *17*, 1863–1879. .

Spinney, L. (2014). Alzheimer's disease: The forgetting gene. Nature *510*, 26–28. .

Szklarczyk, D., Gable, A.L., Lyon, D., Junge, A., Wyder, S., Huerta-Cepas, J., Simonovic, M., Doncheva, N.T., Morris, J.H., Bork, P., et al. (2019). STRING v11: protein-protein association networks with increased coverage, supporting functional discovery in genome-wide experimental datasets. Nucleic Acids Res. *47*, D607–D613. .

Szklarczyk, D., Gable, A.L., Nastou, K.C., Lyon, D., Kirsch, R., Pyysalo, S., Doncheva, N.T., Legeay, M., Fang, T., Bork, P., et al. (2021). The STRING database in 2021: customizable protein-protein networks, and functional characterization of user-uploaded gene/measurement sets. Nucleic Acids Res. *49*, D605–D612. .

Tillo, S.E., Xiong, W.-H., Takahashi, M., Miao, S., Andrade, A.L., Fortin, D.A., Yang, G., Qin, M., Smoody, B.F., Stork, P.J.S., et al. (2017). Liberated PKA Catalytic Subunits Associate with the Membrane via Myristoylation to Preferentially Phosphorylate Membrane Substrates. Cell Rep. *19*, 617–629. .

Tong, L.M., Djukic, B., Arnold, C., Gillespie, A.K., Yoon, S.Y., Wang, M.M., Zhang, O., Knoferle, J., Rubenstein,

J.L.R., Alvarez-Buylla, A., et al. (2014). Inhibitory Interneuron Progenitor Transplantation Restores Normal Learning and Memory in ApoE4 Knock-In Mice without or with Aβ Accumulation. J. Neurosci. *34*, 9506–9515. .

Vizcaíno, J.A., Csordas, A., Del-Toro, N., Dianes, J.A., Griss, J., Lavidas, I., Mayer, G., Perez-Riverol, Y., Reisinger, F., Ternent, T., et al. (2016). 2016 update of the PRIDE database and its related tools. Nucleic Acids Res. *44*, 11033. .

Wang, C., Najm, R., Xu, Q., Jeong, D.-E., Walker, D., Balestra, M.E., Yoon, S.Y., Yuan, H., Li, G., Miller, Z.A., et al. (2018). Gain of toxic apolipoprotein E4 effects in human iPSC-derived neurons is ameliorated by a small-molecule structure corrector. Nat. Med. https://doi.org/10.1038/s41591-018-0004-z.

Wang, Q., Yuan, W., Yang, X., Wang, Y., Li, Y., and Qiao, H. (2020). Role of Cofilin in Alzheimer's Disease. Front Cell Dev Biol *8*, 584898. .

Xu, Q., Walker, D., Bernardo, A., Brodbeck, J., Balestra, M.E., and Huang, Y. (2008). Intron-3 retention/splicing controls neuronal expression of apolipoprotein E in the CNS. J. Neurosci. *28*, 1452–1459. .

Yu, G., Wang, L.-G., Han, Y., and He, Q.-Y. (2012). clusterProfiler: an R package for comparing biological themes among gene clusters. OMICS *16*, 284–287. .

Zhao, J., Fu, Y., Yamazaki, Y., Ren, Y., Davis, M.D., Liu, C.-C., Lu, W., Wang, X., Chen, K., Cherukuri, Y., et al. (2020). APOE4 exacerbates synapse loss and neurodegeneration in Alzheimer's disease patient iPSC-derived cerebral organoids. Nat. Commun. *11*, 5540. .

Zhu, Y., and Hui, D.Y. (2003). Apolipoprotein E binding to low density lipoprotein receptor-related protein-1 inhibits cell migration via activation of cAMP-dependent protein kinase A. J. Biol. Chem. *278*, 36257–36263. .